

Article

# Hydrogenation of $\text{ZnFe}_2\text{O}_4$ Flat Films: Effects of the Pre-Annealing Temperature on the Photoanodes Efficiency for Water Oxidation

Annalisa Polo <sup>1,\*</sup>, Charles R. Lhermitte <sup>2</sup>, Maria Vittoria Dozzi <sup>1</sup>, Elena Selli <sup>1</sup> and Kevin Sivula <sup>2</sup>

<sup>1</sup> Dipartimento di Chimica, Università degli Studi di Milano, via Golgi 19, I-20133 Milano, Italy; mariavittoria.dozzi@unimi.it (M.V.D.); elena.selli@unimi.it (E.S.)

<sup>2</sup> Laboratory for Molecular Engineering of Optoelectronic Nanomaterials, École Polytechnique Federale de Lausanne (EPFL), Station 6, 1015 Lausanne, Switzerland; charles.lhermitte@epfl.ch (C.R.L.); kevin.sivula@epfl.ch (K.S.)

\* Correspondence: annalisa.polo@unimi.it

Received: 25 February 2020; Accepted: 9 March 2020; Published: 12 March 2020



**Abstract:** The effects induced by post-synthesis hydrogenation on  $\text{ZnFe}_2\text{O}_4$  flat films in terms of photoelectrochemical (PEC) performance of photoanodes for water oxidation have been deeply investigated as a function of the pre-annealing temperature of the materials. The structure and morphology of the films greatly affect the efficacy of the post synthesis treatment. In fact, highly compact films are obtained upon pre-annealing at high temperatures, and this limits the exposure of the material bulk to the reductive  $\text{H}_2$  atmosphere, making the treatment largely ineffective. On the other hand, a mild hydrogen treatment greatly enhances the separation of photoproducted charges in films pre-annealed at lower temperatures, as a result of the introduction of oxygen vacancies with n-type character. A comparison between present results and those obtained with  $\text{ZnFe}_2\text{O}_4$  nanorods clearly demonstrates that specific structural and/or surface properties, together with the initial film morphology, differently affect the overall contribution of post-synthesis hydrogenation on the efficiency of zinc ferrite-based photoanodes.

**Keywords:** spinel ferrite; hydrogenation; pre-annealing temperature; PEC performance; transparency; charge transport; flat morphology

## 1. Introduction

The need on Earth for renewable energy is going to rise over the years, driven by the fact that the energy demand of the planet during this century cannot be satisfied by fossil fuels [1]. In this context, the Sun represents a powerful source of freely available energy which could potentially cover more than 10,000 times the global energy need. Therefore, the establishment of scalable and cost effective solar technologies to capture and convert sunlight into electricity or chemical fuels is crucial for the growth of a carbon neutral, renewable, and sustainable global economy [2,3].

Photoelectrochemical (PEC) water splitting is an alternative, cheaper, and competitive route to photovoltaics which allows to store solar energy into hydrogen as flexible chemical fuel, through the consumption of an inexpensive starting material [1,3,4]. Among the different types of PEC devices [5], one of the most efficient is the dual-absorber tandem configuration where two semiconductor electrodes with complementary band gap energies are wired together to maximize light harvesting and cell performance under different conditions [6,7]. In this context, the optical transparency of the first (top) absorber electrode in the wavelength range greater than the material band gap is a requirement to maximize the light absorption efficiency of the device [8,9].

As popular semiconductors to be employed as photoanode materials in this kind of PEC cell, transition metal oxides offer unique advantages, such as facile processability by means of scalable solution-based routes, robustness towards the harsh conditions of water oxidation, relatively narrow band gap energies (1.5–2.3 eV), which are ideal for operation as the top cell in a tandem configuration, and highly oxidizing valence band edges able to drive oxygen evolution [10–14]. Beyond the first generation of binary metal oxides (TiO<sub>2</sub> [15,16], WO<sub>3</sub> [17,18], Fe<sub>2</sub>O<sub>3</sub> [11,19]), the use of the more complex ternary oxides offers the possibility of rationally engineering the band gap structure by tuning the cations composition [10–12,20].

In this frame, metal spinel ferrites (MFe<sub>2</sub>O<sub>4</sub>, M = Ba, Ca, Cu, Co, Mg, Mn, Ni, Zn) have emerged as an attractive class of ternary metal oxides thanks to their abundant constituent elements, visible light harvesting capability, and remarkable thermal and chemical stability [21–25]. In particular, zinc ferrite ZnFe<sub>2</sub>O<sub>4</sub> (ZFO), which shares many of the desired properties of Fe<sub>2</sub>O<sub>3</sub>, including the relatively narrow band gap of 2.0 eV, has been explored as an alternative to such binary oxide [10–12]. However, the performance of ZnFe<sub>2</sub>O<sub>4</sub> photoanodes remained lower compared to that of Fe<sub>2</sub>O<sub>3</sub> despite the many efforts devoted to solve its severe charge recombination issues [11,12].

A benchmark photocurrent density of 1.0 mA cm<sup>-2</sup> under standard testing conditions, i.e., the highest so far recorded using ZnFe<sub>2</sub>O<sub>4</sub> as single absorber photoanode for water oxidation, was reported [22] for ZnFe<sub>2</sub>O<sub>4</sub> electrodes with a nanorod (NR) morphology, upon post-synthesis hydrogenation and cocatalyst deposition. A strong correlation was ascertained between the spinel inversion degree, defined as the fraction of tetrahedral sites occupied by trivalent Fe<sup>3+</sup> ions, and the charge transport in the presence of the peculiar NR morphology. Optimizing this aspect was linked to the observed record PEC performance as a function of the film annealing temperature, which was attained with films after a hydrogenation treatment performed with the aim of improving the n-type character of the photoactive materials [22]. However, how the effects induced by the adopted reductive treatment itself depend on the intrinsic properties of the as prepared materials, and in particular on the electrode pre-annealing temperature, was not investigated.

In this work, the effects induced by this post-synthesis hydrogenation (performed under mild heating conditions) on the PEC performances of ZnFe<sub>2</sub>O<sub>4</sub> photoanodes are systematically studied in relation to the pre-annealing temperature employed in their synthesis. We focus on ZnFe<sub>2</sub>O<sub>4</sub> flat films as ideal models to investigate the effects produced by reductive hydrogen atmosphere with the main aim of enhancing the overall film electron conductivity through the introduction of oxygen vacancies acting as n-type dopants [23,26–28]. In addition, we demonstrate that the particular temperature adopted during the synthetic thermal treatment of ZnFe<sub>2</sub>O<sub>4</sub> not only affects the final performance of unmodified flat films, but also ensures different PEC efficiency increases upon the application of the same hydrogen treatment. The multiple factors which may be at the origin of the different trends in PEC performance in relation to the annealing temperature detected for pristine and hydrogenated ZnFe<sub>2</sub>O<sub>4</sub> films are investigated here and deeply discussed. In particular, since we aimed to exclude the potential effects induced by film thickness on the poor charge transport properties, we focus on the investigation of flat ZFO films with moderate thickness, i.e., ca. 100 nm thick, prepared according to a generalized approach for ternary metal oxides, which offers a facile processable green route to obtain optically transparent films suitable to be employed as photoanodes in dual absorber tandem PEC cells.

## 2. Materials and Methods

### 2.1. Chemicals and Materials

The following chemicals were employed. Zn(NO<sub>3</sub>)<sub>6</sub>·6H<sub>2</sub>O was purchased from ABCR (Zug, Switzerland), Fe(NO<sub>3</sub>)<sub>3</sub>·9H<sub>2</sub>O was supplied by Acros Organics (Wohlen, Switzerland), HNO<sub>3</sub> and NH<sub>4</sub>OH (25%) were purchased from VWR (Dietikon, Switzerland) and NaOH was provided by Reactolab SA (Servion, Switzerland). Ethylenediaminetetraacetic acid (EDTA) was purchased from (Fluka, Buchs, Switzerland). The used substrate was FTO coated aluminoborosilicate glass (Solaronix).

## 2.2. Photoelectrodes Preparation

The ZnFe<sub>2</sub>O<sub>4</sub> photoanodes were synthesized via spin coating and subsequent annealing. In order to prepare the ZnFe<sub>2</sub>O<sub>4</sub> precursor solution, 10.959 g (1.5 eq.) EDTA was initially dissolved into 50 mL of 18.2 MΩ resistance (Millipore, Schaffhausen, Switzerland) water upon addition of 5 mL of fresh 25% NH<sub>4</sub>OH solution. To allow the complete dissolution of EDTA, the solution mixture was maintained under continuous stirring for about 30 min. Then, 10.1 g (1 eq.) of Fe(NO<sub>3</sub>)<sub>3</sub>·9H<sub>2</sub>O was added, causing the formation of a white precipitate which was suspected to be EDTA that precipitated from solution due to the decrease in pH upon adding the acidic Fe(NO<sub>3</sub>). The precipitate was dissolved upon addition of 5 mL of the 25% NH<sub>4</sub>OH solution. Finally, 3.786 g (1 eq.) of Zn(NO<sub>3</sub>)<sub>2</sub>·6H<sub>2</sub>O was dissolved into the mixture by adding the 25% NH<sub>4</sub>OH solution until the solution pH was 5. The solution was then heated at 60 °C under stirring for 1 h until all the solids had dissolved and no precipitate was visibly detected. Once cooled to room temperature, the final solution pH was brought back to 5 by adding diluted HNO<sub>3</sub> or NH<sub>4</sub>OH solutions and the final volume was adjusted to 100 mL by water addition. The final solution was 0.25 M in Fe<sup>3+</sup>, 0.125 M in Zn<sup>2+</sup> and 0.375 M in EDTA, and was stable for several months.

Prior to deposition, the FTO substrates were cleaned thoroughly with four 15 min long sonication cycles in a soap/water mixture, acetone, ethanol, and finally in distilled water. The cleaned substrates then underwent plasma cleaning for 15 min.

The Fe<sup>3+</sup>- and Zn<sup>2+</sup>-containing solution was deposited onto the clean FTO coated glass substrate through spin coating using a dynamic technique where the substrate was first spun at 4500 rpm. Once the substrate was at this speed, 0.75 mL of the previously prepared solution was deposited on top while keeping the electrode spinning for 45 s to allow the solution to homogeneously distribute over the FTO substrate.

The thin films were then calcined at 400 °C in air to burn off all organic materials. The deposition and calcination procedures were repeated 20 times in order to obtain electrodes of the desired thickness. The films were then annealed for 20 min in a preheated tubular furnace at different temperatures, i.e., at 500 °C, 600 °C, 700 °C, and 800 °C, followed by cooling down to room temperature with the furnace off. The obtained samples were labelled as 20L\_X, where X refers to the annealing temperature in Celsius.

To increase the film conductivity, the prepared electrodes underwent a post synthesis hydrogenation treatment in a tubular furnace at 200 °C for 60 min under H<sub>2</sub> atmosphere. These samples were named 20L\_X\_H<sub>2</sub>.

A series of thinner films was also prepared by the same way, starting from a 0.50 M in Fe<sup>3+</sup>, 0.25 M in Zn<sup>2+</sup> and 0.75 M in EDTA precursor solution. The deposition of the so obtained “doubly concentrated ZFO precursor solution” (DC) onto clean FTO was repeated 5 times by maintaining the same pre-annealing treatment at 400 °C between each deposition step and the same final thermal treatment for 20 min at 500 °C or 800 °C. These films were also subjected to the previously described post synthesis hydrogen treatment. These two series of films were referred to as DC\_5L\_X and DC\_5L\_X\_H<sub>2</sub>, with X referring to the annealing temperature in Celsius.

## 2.3. Structural, Morphological and Optical Characterizations

The crystal structure and phase composition of all synthesized 20L ZFO films was assessed by means of X-ray diffraction (XRD) and Raman spectroscopy analyses. For investigating the crystalline phase of the materials, a Panalytical Empyrean system (Theta-Theta, 240 mm, Malvern, UK) was employed, equipped with a PIXcel-1D detector (Malvern, UK), Bragg-Brentano beam optics (including a hybrid monochromator, INTEGRATED Engineering Software, Winnipeg, Canada), and parallel beam optics. Raman spectra were collected with a LabRam spectrometer (Jobin Yvon Horiba, Bensheim, Germany). SEM images were acquired using a Zeiss Gemini 300 scanning electron microscope (Jena, Germany) in the HV mode. The excitation line was provided by an Ar laser (532.19 nm, Jena, Germany). UV-visible absorption spectra were recorded in the transmission mode in a UV-3600 Shimadzu spectrometer (Duisburg, Germany).

## 2.4. Photoelectrochemical Tests

PEC experiments were carried out using a three-electrode cappuccino cell [29] connected to a BioLogic SP-500 potentiostat (Seyssinet-Pariset, France). The  $\text{ZnFe}_2\text{O}_4$  films were used as working electrode, while an Ag/AgCl (3.0 M NaCl) electrode and a Pt wire were used as reference and counter electrode, respectively. The light source was a 1000 W Xe arc lamp (Newport Oriel) calibrated using a Si photodiode to provide a  $100 \text{ mW cm}^{-2}$  light intensity and a photon flux corresponding to the AM 1.5 G spectrum for energy larger than the band gap of the tested material [30]. The investigated electrodes were tested as photoanodes in Linear Sweep Voltammetry (LSV) measurements under both back (through the FTO glass substrate side) and front (through the deposited film side) irradiation configurations, in contact with a 1.0 M NaOH aqueous solution (pH 14). The acquired potential vs. Ag/AgCl values were converted into the RHE scale using the following equation:  $E_{\text{RHE}} = E_{\text{AgCl}} + 0.059 \text{ pH} + E^0_{\text{AgCl}}$ , with  $E^0_{\text{AgCl}}$  (3.0 M NaCl) = 0.210 V at 25 °C.

## 3. Results

### 3.1. Photoelectrodes Characterization

The XRD patterns and Raman spectra recorded for all investigated 20L\_X samples are shown in Figure 1. The diffractograms shown in Figure 1a display only the (220), (311), and (511) reflections associated to the spinel ferrite cubic structure (Fd3m space group) and to the FTO substrate, indicating that no signals related to any segregated (binary oxide) phases are detectable [22]. The crystallinity of the ZFO films appears to be strongly correlated to the synthesis temperature, as demonstrated by the peak intensity increase with increasing annealing temperature, particularly evident for the (311) reflection, in agreement with previous results obtained with NR films [22].

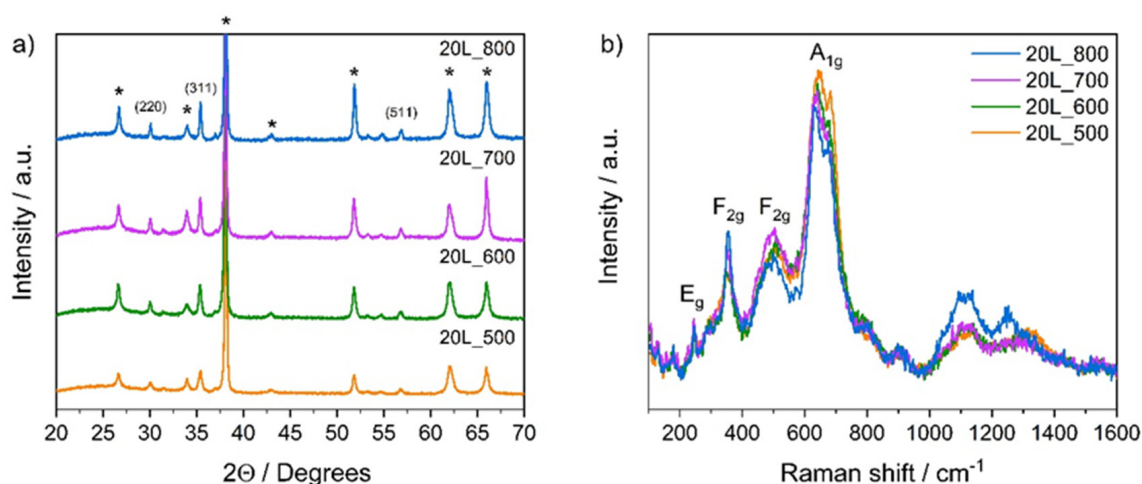


**Figure 1.** (a) X-ray diffraction (XRD) patterns and (b) Raman spectra of the 20L films annealed at different temperatures. Reflections originated from the FTO substrate are indicated by asterisks.

The Raman spectra of the same films (Figure 1b) were also collected in order to confirm the formation of a crystal phase without the presence of secondary phases. All Raman spectra exhibit the characteristic Raman modes of ZFO [31], i.e.,  $E_g$  at  $245 \text{ cm}^{-1}$ ,  $F_{2g}$  at  $355 \text{ cm}^{-1}$  and  $505 \text{ cm}^{-1}$  and  $A_{1g}$  centred at  $650 \text{ cm}^{-1}$ . The lack of the intense  $1320 \text{ cm}^{-1}$  centered band typical of hematite ( $\alpha\text{-Fe}_2\text{O}_3$ ) [32] and of the broad feature at  $1400 \text{ cm}^{-1}$  relative to maghemite ( $\gamma\text{-Fe}_2\text{O}_3$ ) [33] corroborates the absence of these impurity phases in the synthesized spinel ferrite electrodes, while the presence of traces of magnetite ( $\text{Fe}_3\text{O}_4$ ), with bands at  $500 \text{ cm}^{-1}$  and  $679 \text{ cm}^{-1}$  [34], superimposed to the ZFO Raman features, cannot be completely excluded. The same phase composition and purity was identified in the

Raman spectra relative to the thinner DC\_5L films (not shown for the sake of brevity) indicating the growth of a monophasic spinel ferrite also in this case.

The scanning electron microscopy analysis of the 20L\_800 sample, shown in Figure 2, demonstrates a flat film morphology, composed of densely packed, interconnected nanoparticles (Figure 2a). Cross sectional SEM images (Figure 2b) indicate that the films are approximately 100 nm thick.

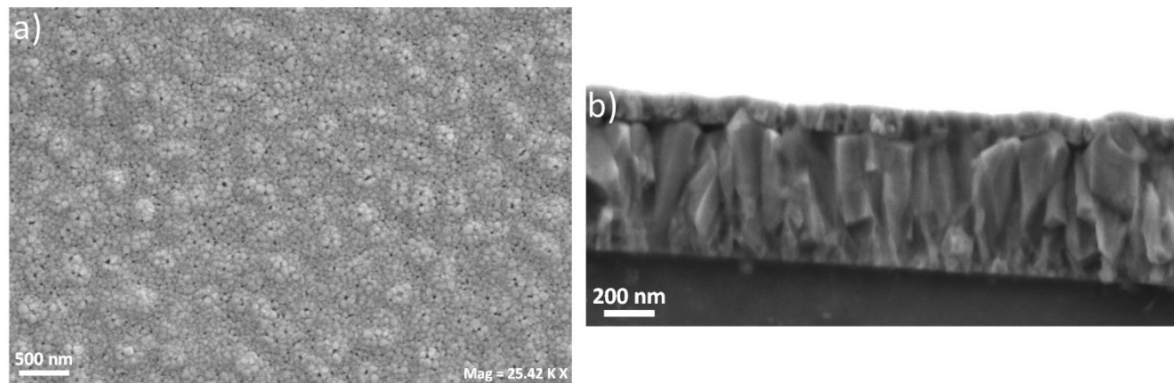


**Figure 2.** (a) Top down and (b) cross section SEM images of the 20L\_800 film.

The absorbance spectra of both 20L\_X and DC\_5L\_X film series are reported in Figure 3. Both electrode series exhibit high optical transparency in the wavelength range above the absorption onset of the material (ca. 620 nm in agreement with a band gap energy of 2.0 eV), which is characterized by the presence of interference fringes due to the flatness of the investigated thin films. The high level of film transparency can be also appreciated in the inset of Figure 3. The 20L samples exhibit a ca. 1.7-fold higher absorbance with respect to that observed with DC\_5L films, thus confirming their relatively higher thickness. Within each series the change of film annealing temperature does not produce any significant variation in terms of either UV-vis absorption capability or ZFO nanoparticles interconnection.

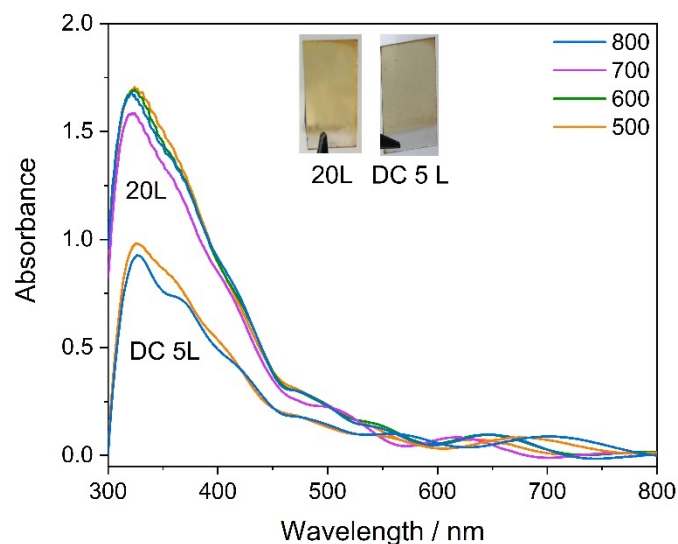


**Figure 3.** Absorbance spectra of the 20L and DC\_5L films series annealed at different temperatures (in Celsius).

The 20L and DC\_5L films annealed at 800 °C showed significantly different surface topography, as evidenced by the AFM analyses reported in Figure 4. In the case of 20L films, the higher number of layer depositions, requiring a 400 °C treatment at each intermediate step, caused the formation of a quite smooth surface consisting of densely aggregated small grains (Figure 4b). On the other hand, the fewer deposition steps used for producing the thinner DC\_5L\_800 sample drastically change the

film topography, which appears mainly composed of sharper grains with a ridge shape (Figure 4a) possibly resulting from the underlying FTO substrate. Indeed, the DC\_5L film is characterized by a higher surface roughness with respect to the corresponding 20L electrode, as demonstrated by the relative root mean square (RMS) roughness factors reported in Figure 4 for each film.

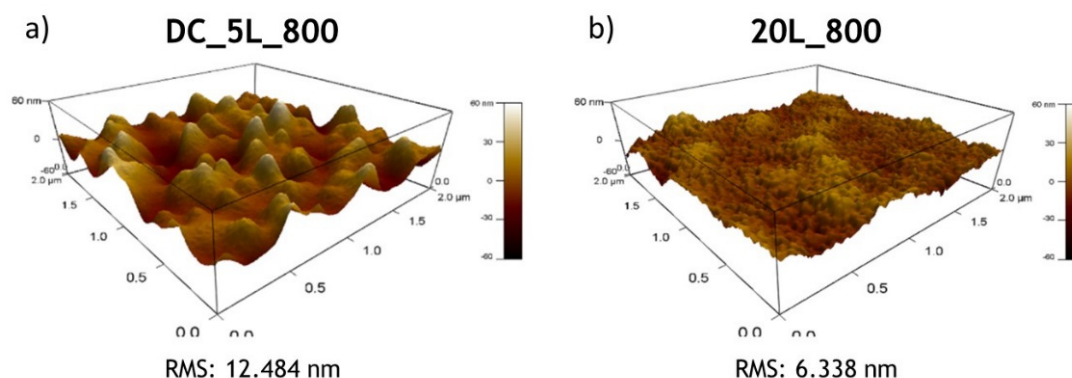


**Figure 4.** AFM images and root mean square (RMS) factors for the (a) DC\_5L\_800 and (b) 20L\_800 films.

### 3.2. Photoelectrochemical Performance

The PEC performance of all synthesized 20L and DC\_5L films was checked in a 1.0 M NaOH solution. The results of the tests performed with the pristine 20L\_800 are reported as an example in Figure 5a. The comparison of the photocurrent vs. voltage (J-V) curves recorded in Linear Sweep Voltammetry (LSV) scans under irradiation through the ZFO/water interface of the film (front side irradiation) or through the glass substrate side (back side irradiation) indicates a progressively higher photocurrent density for back-side illumination rather than front-side illumination. Thus, the photogenerated charge separation in the bulk is more efficient when the majority charge carriers, electrons in the case of a n-type semiconductors [35] as ZFO, are generated close to the back FTO contact where they can be directly transferred to the conductive substrate. This supports the notion that electron transport through the bulk of the film towards the FTO substrate is more limiting than hole transport towards the film/electrolyte interface.

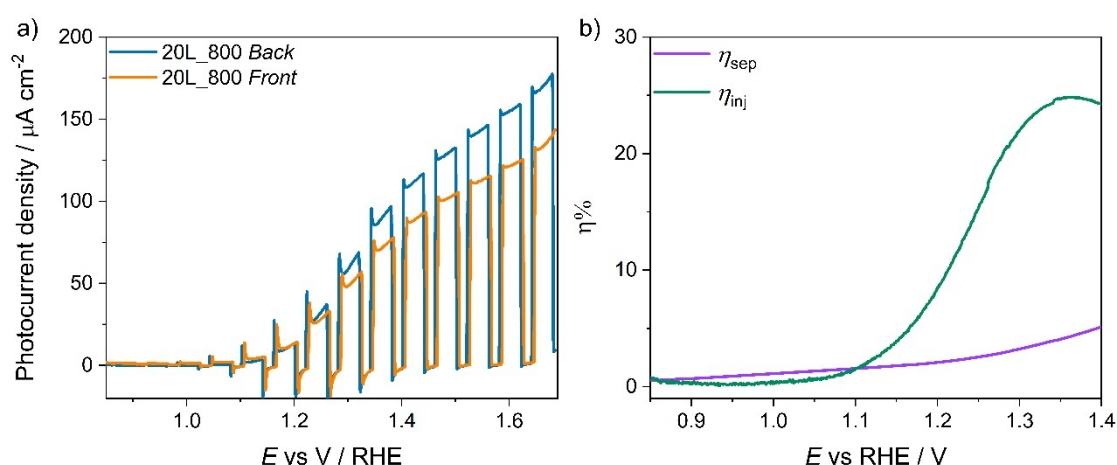


**Figure 5.** (a) Linear Sweep Voltammetry (LSV) plots relative to the 20L\_800 °C film in 1.0 M NaOH under both back and front side irradiation configurations. (b) Charge separation ( $\eta_{sep}$ ) and charge injection efficiencies ( $\eta_{inj}$ ) calculated for the same film.

The need for a hydrogenation treatment, aiming to improve the majority charge carriers transport through the introduction of oxygen vacancies, was assessed by calculating the charge separation and

charge injection efficiencies [23,26–28]. To this aim, the PEC performance of the 20L\_800 film was also investigated in the presence of  $\text{H}_2\text{O}_2$  as hole scavenger in the 1.0 M NaOH electrolyte.

The photocurrent density produced during water oxidation can be expressed as  $J_{\text{H}_2\text{O}} = J_{\text{abs}} \cdot \eta_{\text{sep}} \cdot \eta_{\text{inj}}$ , where  $J_{\text{abs}}$  is the theoretical maximum photocurrent density calculated by converting the absorbed photons into current,  $\eta_{\text{sep}}$  the charge separation yield of the photogenerated carriers, and  $\eta_{\text{inj}}$  the minority charge carriers injection yield at the film/electrolyte interface [19].  $J_{\text{abs}}$  was calculated as  $7.38 \text{ mA cm}^{-2}$ , by integrating the absorption spectrum of the investigated film on the AM 1.5 G solar spectrum. Using a hole scavenger such as  $\text{H}_2\text{O}_2$ , for which a 100% charge injection yield can be assumed (i.e.,  $\eta_{\text{inj}} = 1$ ) [19,36], the charge separation efficiency  $\eta_{\text{sep}}$  was calculated from the photocurrent density measured in the presence of  $\text{H}_2\text{O}_2$  under such conditions  $J_{\text{H}_2\text{O}_2} = J_{\text{abs}} \cdot \eta_{\text{sep}}$ . Moreover, the hole injection efficiency for pure water oxidation was finally obtained as the ratio between  $J_{\text{H}_2\text{O}}$  and  $J_{\text{H}_2\text{O}_2}$ .

As shown in Figure 5b, a very low  $\eta_{\text{sep}}$  (below 10%) was obtained, while higher  $\eta_{\text{inj}}$  values were recorded above 1.1 V vs. RHE up to 25% charge injection efficiency attained around 1.35 V vs. RHE. This means that the material performance is mainly limited by an inefficient charge separation in the bulk, which could be improved by a reductive treatment under  $\text{H}_2$  atmosphere.

Figure 6 shows the J-V curves recorded in 1.0 M NaOH under back side irradiation and the corresponding dark scans relative to the 20L\_X and 20L\_X\_ $\text{H}_2$  samples thermally treated at the lowest (500 °C, Figure 6a) or at the highest (800 °C, Figure 6b) temperature. First, no detectable contribution from the dark scan to the recorded photoactivity can be observed for all electrodes in the whole investigated potential window. By comparing the performance relative to the two different pristine films, a better fill factor resulting in a 2.4-fold enhancement of photocurrent density recorded at 1.5 V vs. RHE was attained by increasing the ZFO film annealing temperature from 500 °C to 800 °C. This should be clearly related to the higher crystallinity degree attained by pre-annealing at higher temperature. On the contrary, the gain in performance upon reduction by hydrogen treatment is incredibly higher in the case of the ZFO film annealed at 500 °C. In fact, 20L\_500\_ $\text{H}_2$  shows either a better fill factor or a better photocurrent onset compared to the corresponding untreated 20L\_500 electrode, resulting in a five-fold higher photocurrent density of  $230 \text{ } \mu\text{A cm}^{-2}$  at 1.5 V vs. RHE for the so optimized photoanode (Figure 6a).

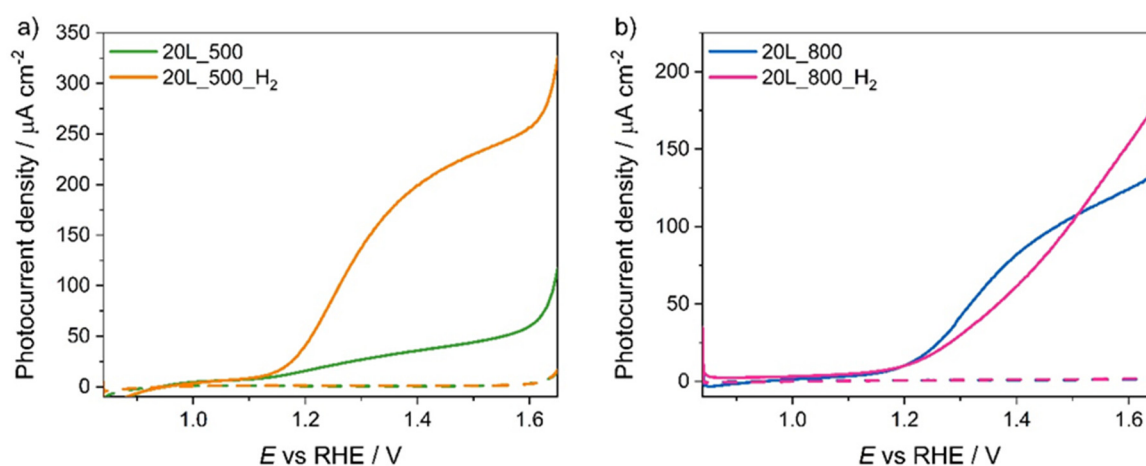


**Figure 6.** Linear Sweep Voltammetry (LSV) plots of the films annealed at (a) 500 °C and (b) 800 °C, before and after the hydrogenation treatment. Dashed lines refer to the recorded dark currents.

However, hydrogenation does not produce the same effect when performed on the 20L\_800 film. As shown in Figure 6b, only a slight photocurrent density enhancement was recorded above 1.5 V vs. RHE upon hydrogenation of the pristine 20L\_800 film. Moreover, a worse photocurrent onset, accompanied by a lower fill factor, was induced by the reductive treatment.

The effects of the hydrogenation treatment vs. the adopted pre-annealing temperature, enduring for several months, can be appreciated in Figure 7, reporting the photocurrent density values recorded at the fixed applied potential of 1.5 V vs. RHE for all investigated electrodes as a function of their pre-annealing temperature. Two opposite trends can be observed for the films in their pure and hydrogenated forms. While in the case of pristine electrodes an increase in photocurrent density occurs with increasing pre-annealing temperature, a progressive drop in performance with increasing pre-annealing temperature characterizes the materials after hydrogenation. For the two films series, the photocurrent density is almost constantly moving from 500 °C to 600 °C, while it sharply changes when raising the pre-annealing temperature from 700 °C to 800 °C. The observed photoactivity increase for the pristine electrodes can be reasonably correlated to the increase in the material crystallinity with increasing pre-annealing temperature [22]. In fact, in highly crystalline materials trapping of photogenerated charge carriers on lattice disorder sites is prevented [37], resulting in a relatively low charge transfer resistance in the bulk and consequently enhanced charge separation [38]. For the untreated pristine films, this resulted in a photocurrent enhancement with increasing annealing temperature so that no detectable improvement was observed upon hydrogenation of highly crystalline films already endowed with excellent charge separation properties.

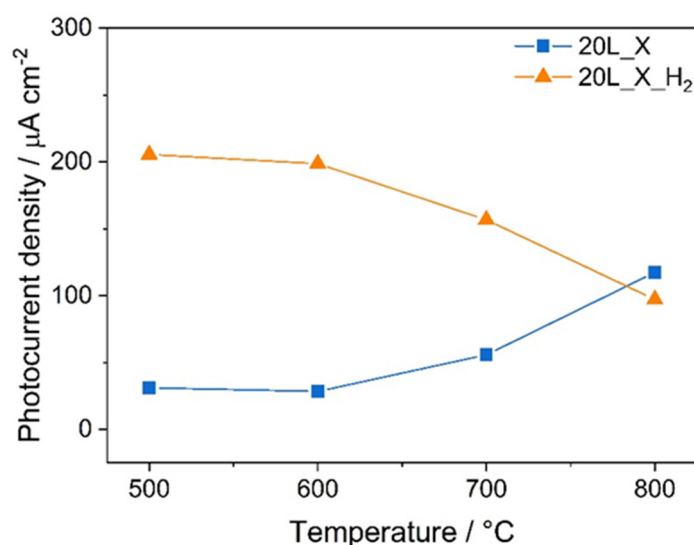


**Figure 7.** Photocurrent density measured with the 20L films at 1.5 V vs. RHE as a function of the annealing temperature.

However, other factors could also account for the photoactivity drop with increasing pre-annealing temperature observed for the hydrogenated films. For example, the ca 100 nm thickness of the 20L film series should not be sufficient to appreciate the beneficial effect of the reduction treatment when the material conductivity is good enough due to the significant crystallinity degree imparted by the high pre-annealing temperature. Moreover, the 20L structure combined with pre-annealing at 800 °C also produces highly compact films as shown by the AFM image in Figure 4b, which may hamper efficient exposure of the bulk material to hydrogen, especially when the film surface has a flat morphology.

To identify the main reason of the ineffectiveness of hydrogenation in combination with the high annealing temperature of 20L films, we also tested the performance of thinner DC\_5L films annealed at 500 °C and 800 °C. Figure 8 reports the J-V curves acquired with these materials under back side AM 1.5 G irradiation. As shown, the beneficial effect induced on the PEC performance of the pristine films by the higher crystallinity of the materials annealed at 800 °C was confirmed in the case of the thinner DC\_5L\_800 electrode vs. the DC\_5L\_500 film. However, a different photoactivity improvement trend occurred upon hydrogenation of thinner DC\_5L films with respect to the 20L electrode series. In fact, the DC\_5L\_800 electrode exhibits higher photocurrent density compared to the DC\_5L\_500 film even

after the hydrogenation treatment, in addition to the six-fold photocurrent enhancement at 1.5 V vs. RHE with respect to the pristine DC\_5L\_800 photoanode.

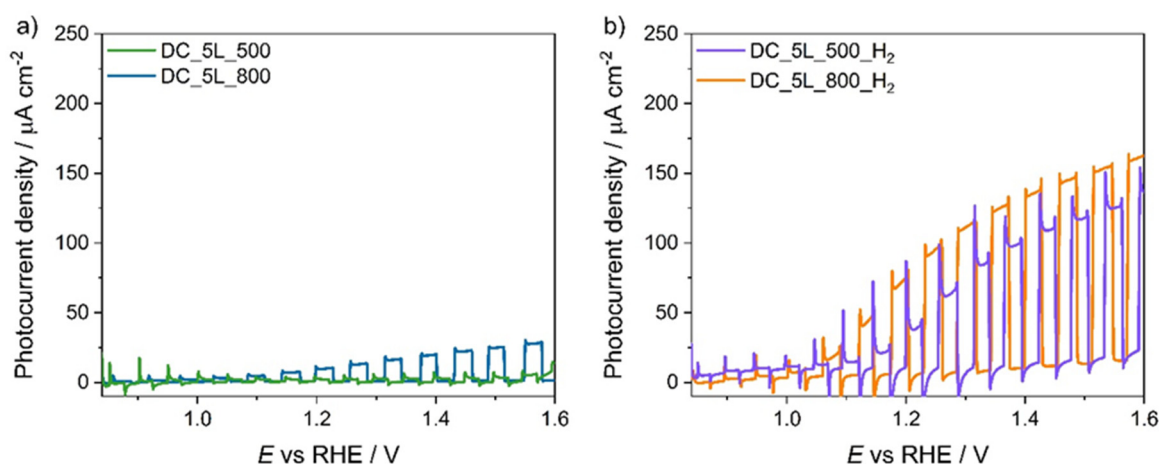


**Figure 8.** Linear Sweep Voltammetry (LSV) plots of DC\_5L\_500 and DC\_5L\_800 films (a) before and (b) after hydrogenation.

This means that the beneficial effect induced by hydrogenation in favoring bulk charge transport properties can be attained also for a highly crystalline and performant starting material (annealed at 800 °C) with a thickness below 100 nm. Thus, the higher thickness of 20L films is not the main reason for the lack of PEC performance improvement of 20L\_800 upon hydrogenation. In fact, post-synthesis mild hydrogenation promotes even the PEC performance of an efficient material, such as DC\_5L\_800, the performance of which is not expected to be affected by charge transportation limitations due to its low thickness and high crystallinity. The highly compact structure of the 20L\_800 film may instead be at the origin of its ineffective exposition to H<sub>2</sub> with a consequently limited bulk oxygen vacancies production.

Thus, in order to maximize the PEC performance of ZFO flat materials by exploiting both the intrinsic charge carrier separation capability of a highly crystalline structure and the further enhanced charge conductivity induced by oxygen vacancy introduction, the starting ZFO flat film has to be annealed at a relatively high temperature and expose a high surface area together with a less compact structure, able to promote H<sub>2</sub> penetration into its bulk structure. In fact, the hydrogenation efficiency itself strongly depends on the annealing temperature, which in turn affects the compactness of the film structure and its permeability towards hydrogenation.

In particular, we propose a synthetic strategy aiming at promoting the PEC properties of ZFO films with flat morphology. In order to maximize their efficiency as photoanodes it is thus recommended to apply a hydrogenation treatment to films prepared in a multilayer structure of at least 100 nm thickness (20L series), previously annealed at low temperature (500 °C). At the same time, to approach such maximum performance by following a much more time-saving synthetic route, the same H<sub>2</sub> treatment should be performed for thinner ZFO films (DC\_5L series) annealed at high temperatures (800 °C).

Potential synergistic effects induced by combining hydrogenation and multiple synthetic parameters (i.e., annealing temperature, number of deposited layers, and structure compactness) have been systematically studied, thus paving out a way for designing more efficient ZFO-based flat films to be employed as photoanodes for O<sub>2</sub> production from water oxidation.

#### 4. Conclusions

The efficiency of hydrogenation of ZFO photoanodes in terms of enhanced PEC performance strongly depends on the annealing temperature of the starting material, being maximum for 20L films annealed at relatively low temperatures (500 °C), while an increasing drop in performance occurs with increasing pre-annealing temperature. We ascribed the enhanced photocurrent upon hydrogen treatment of films previously annealed at low temperatures (500–600 °C) to the improved charge

separation properties thanks to the n-type character of the induced oxygen vacancies. On the other hand, the decrease in hydrogenation efficiency with the rise in temperature can be due to the inefficient exposure of the material bulk to the reductive H<sub>2</sub> flux when the film presents a compact structure, as a consequence of the combined high pre-annealing temperature and multilayer structure, and a low surface area because of its flat morphology. These insights point to the effectiveness of films with high surface areas as in the case of the NR morphology, which is known to perform the best for this material. Thus, future efforts at enhancing the performance of the ZFO material in flat form should focus on films with a less compact structure and higher surface area, to fully exploit the efficacy of the H<sub>2</sub> treatment.

**Author Contributions:** K.S. provided a supervision of both experiments and data interpretation; C.R.L. provided the synthesis procedure and performed the electron microscopy analyses; A.P. performed all experiments and data analyses, wrote a draft of the paper, and contributed to its revision; M.V.D. and E.S. contributed in writing and optimizing the final version of the manuscript. All authors have read, provided corrections and finally agreed to the submitted version of the manuscript.

**Funding:** This research was partially funded by the Swiss Competence Centers for Energy Research (SCCER) Heat and Electricity Storage Consortium, KTI contract number [1155002545].

**Acknowledgments:** The collaboration of Pascal Schouwink, Institute of Chemical Sciences and Engineering (ISIC), EPFL, Lausanne (Switzerland), in XRD analysis is gratefully acknowledged. Jun Ho Yum from the Laboratory for Molecular Engineering of Optoelectronic Nanomaterials (LIMNO), EPFL, Lausanne (Switzerland) is acknowledged for AFM images acquisition.

**Conflicts of Interest:** The authors declare no conflict of interest.

## References

1. Grätzel, M. Photoelectrochemical cells. *Nature* **2001**, *414*, 338–344. [[CrossRef](#)]
2. Lewis, N.S. Research opportunities to advance solar energy utilization. *Science* **2016**, *351*, 1920. [[CrossRef](#)] [[PubMed](#)]
3. Walter, M.G.; Warren, E.L.; McKone, J.R.; Boettcher, S.W.; Mi, Q.; Santori, E.A.; Lewis, N.S. Solar Water Splitting Cells. *Chem. Rev.* **2010**, *110*, 6446–6473. [[CrossRef](#)] [[PubMed](#)]
4. Bard, A.J. Design of semiconductor photoelectrochemical systems for solar energy conversion. *J. Phys. Chem.* **1982**, *86*, 172–177. [[CrossRef](#)]
5. Nielander, A.C.; Shaner, M.R.; Papadantonakis, K.M.; Francis, S.A.; Lewis, N.S. A taxonomy for solar fuels generators. *Energy Environ. Sci.* **2015**, *8*, 16–25. [[CrossRef](#)]
6. Prévot, M.S.; Sivula, K. Photoelectrochemical Tandem Cells for Solar Water Splitting. *J. Phys. Chem. C* **2013**, *117*, 17879–17893. [[CrossRef](#)]
7. Khaselev, O.; Turner, J.A. A Monolithic Photovoltaic-Photoelectrochemical Device for Hydrogen Production via Water Splitting. *Science* **1998**, *280*, 425–427. [[CrossRef](#)] [[PubMed](#)]
8. Prévot, M.S.; Li, Y.; Guijarro, N.; Sivula, K. Improving charge collection with delafossite photocathodes: A host–guest CuAlO<sub>2</sub>/CuFeO<sub>2</sub> approach. *J. Mater. Chem. A* **2016**, *4*, 3018–3026. [[CrossRef](#)]
9. Lhermitte, C.R.; Polo, A.; Yao, L.; Boudoire, F.A.; Guijarro, N.; Sivula, K. Generalized Synthesis for the Production of Transparent Thin Films of Ternary Metal Oxide Electrodes. Unpublished.
10. Abdi, F.F.; Berglund, S.P. Recent developments in complex metal oxide photoelectrodes. *J. Phys. D Appl. Phys.* **2017**, *50*, 193002. [[CrossRef](#)]
11. Sivula, K.; van de Krol, R. Semiconducting materials for photoelectrochemical energy conversion. *Nat. Rev. Mater.* **2016**, *1*. [[CrossRef](#)]
12. Lee, D.K.; Lee, D.; Lumley, M.A.; Choi, K.S. Progress on ternary oxide-based photoanodes for use in photoelectrochemical cells for solar water splitting. *Chem. Soc. Rev.* **2019**, *48*, 2126–2157. [[CrossRef](#)] [[PubMed](#)]
13. Buriak, J.M.; Toro, C.; Choi, K.S. Chemistry of Materials for Water Splitting Reactions. *Chem. Mater.* **2018**, *30*, 7325–7327. [[CrossRef](#)]
14. Lhermitte, C.R.; Sivula, K. Alternative Oxidation Reactions for Solar-Driven Fuel Production. *ACS Catal.* **2019**, *9*, 2007–2017. [[CrossRef](#)]
15. Dozzi, M.V.; Selli, E. Doping TiO<sub>2</sub> with p-block elements: Effects on photocatalytic activity. *J. Photochem. Photobiol. C Photochem. Rev.* **2013**, *14*, 13–28. [[CrossRef](#)]
16. Polo, A.; Grigioni, I.; Dozzi, M.V.; Selli, E. Sensitizing effects of BiVO<sub>4</sub> and visible light induced production of highly reductive electrons in the TiO<sub>2</sub>/BiVO<sub>4</sub> heterojunction. *Catal. Today* **2020**, *340*, 19–25. [[CrossRef](#)]

17. Lhermitte, C.R.; Garret Verwer, J.; Bartlett, B.M. Improving the stability and selectivity for the oxygen-evolution reaction on semiconducting WO<sub>3</sub> photoelectrodes with a solid-state FeOOH catalyst. *J. Mater. Chem. A* **2016**, *4*, 2960–2968. [[CrossRef](#)]
18. Grigioni, I.; Abdellah, M.; Corti, A.; Dozzi, M.V.; Hammarström, L.; Selli, E. Photoinduced Charge-Transfer Dynamics in WO<sub>3</sub>/BiVO<sub>4</sub> Photoanodes Probed through Midinfrared Transient Absorption Spectroscopy. *J. Am. Chem. Soc.* **2018**, *140*, 14042–14045. [[CrossRef](#)]
19. Dotan, H.; Sivula, K.; Grätzel, M.; Rothschild, A.; Warren, S.C. Probing the photoelectrochemical properties of hematite ( $\alpha$ -Fe<sub>2</sub>O<sub>3</sub>) electrodes using hydrogen peroxide as a hole scavenger. *Energy Environ. Sci.* **2011**, *4*, 958–964. [[CrossRef](#)]
20. Lhermitte, C.R.; Bartlett, B.M. Advancing the Chemistry of CuWO<sub>4</sub> for Photoelectrochemical Water Oxidation. *Acc. Chem. Res.* **2016**, *49*, 1121–1129. [[CrossRef](#)]
21. de Haart, L.G.J.; Blasse, G. Photoelectrochemical Properties of Ferrites with the Spinel Structure. *J. Electrochem. Soc.* **1985**, *132*, 2933–2938. [[CrossRef](#)]
22. Zhu, X.; Guijarro, N.; Liu, Y.; Schouwink, P.; Wells, R.A.; Le Formal, F.; Sun, S.; Gao, C.; Sivula, K. Spinel structural disorder influences solar-water-splitting performance of ZnFe<sub>2</sub>O<sub>4</sub> nanorod photoanodes. *Adv. Mater.* **2018**, *30*, 1–6. [[CrossRef](#)] [[PubMed](#)]
23. Guijarro, N.; Bornoz, P.; Prévot, M.; Yu, X.; Zhu, X.; Johnson, M.; Jeanbourquin, X.; Le Formal, F.; Sivula, K. Evaluating spinel ferrites MFe<sub>2</sub>O<sub>4</sub> (M = Cu, Mg, Zn) as photoanodes for solar water oxidation: Prospects and limitations. *Sustain. Energy Fuels* **2018**, *2*, 103–117. [[CrossRef](#)]
24. Dillert, R.; Taffa, D.H.; Wark, M.; Bredow, T.; Bahnemann, D.W. Research Update: Photoelectrochemical water splitting and photocatalytic hydrogen production using ferrites (MFe<sub>2</sub>O<sub>4</sub>) under visible light irradiation. *APL Mater.* **2015**, *3*, 104001. [[CrossRef](#)]
25. Prévot, M.S.; Jeanbourquin, X.A.; Bourée, W.S.; Abdi, F.; Friedrich, D.; van de Krol, R.; Guijarro, N.; Le Formal, F.; Sivula, K. Evaluating Charge Carrier Transport and Surface States in CuFeO<sub>2</sub> Photocathodes. *Chem. Mater.* **2017**, *29*, 4952–4962. [[CrossRef](#)]
26. Kim, J.H.; Jang, Y.J.; Kim, J.H.; Jang, J.W.; Choi, S.H.; Lee, J.S. Defective ZnFe<sub>2</sub>O<sub>4</sub> nanorods with oxygen vacancy for photoelectrochemical water splitting. *Nanoscale* **2015**, *7*, 19144–19151. [[CrossRef](#)]
27. Zhao, X.; Feng, J.; Chen, S.; Huang, Y.; Sum, T.C.; Chen, Z. New insight into the roles of oxygen vacancies in hematite for solar water splitting. *Phys. Chem. Chem. Phys.* **2017**, *19*, 1074–1082. [[CrossRef](#)]
28. Rioult, M.; Stanescu, D.; Fonda, E.; Barbier, A.; Magnan, H. Oxygen Vacancies Engineering of Iron Oxides Films for Solar Water Splitting. *J. Phys. Chem. C* **2016**, *120*, 7482–7490. [[CrossRef](#)]
29. Liu, Y.; Le Formal, F.; Boudoire, F.; Yao, L.; Sivula, K.; Guijarro, N. Insights into the interfacial carrier behaviour of copper ferrite (CuFe<sub>2</sub>O<sub>4</sub>) photoanodes for solar water oxidation. *J. Mater. Chem. A* **2019**, *7*, 1669–1677. [[CrossRef](#)]
30. Prévot, M.S.; Guijarro, N.; Sivula, K. Enhancing the Performance of a Robust Sol–Gel-Processed p-Type Delafossite CuFeO<sub>2</sub> Photocathode for Solar Water Reduction. *ChemSusChem* **2015**, *8*, 1359–1367. [[CrossRef](#)]
31. Wang, Z.; Schiferl, D.; Zhao, Y.; O'Neill, H.S.C. High pressure Raman spectroscopy of spinel-type ferrite ZnFe<sub>2</sub>O<sub>4</sub>. *J. Phys. Chem. Solids* **2003**, *64*, 2517–2523. [[CrossRef](#)]
32. Bourée, W.S.; Prévot, M.S.; Jeanbourquin, X.A.; Guijarro, N.; Johnson, M.; Formal, F.L.; Sivula, K. Robust Hierarchically Structured Biphasic Ambipolar Oxide Photoelectrodes for Light-Driven Chemical Regulation and Switchable Logic Applications. *Adv. Mater.* **2016**, *28*, 9308–9312. [[CrossRef](#)] [[PubMed](#)]
33. Chaudhari, N.S.; Warule, S.S.; Muduli, S.; Kale, B.B.; Jouen, S.; Lefez, B.; Hannoyer, B.; Ogale, S.B. Maghemite (hematite) core (shell) nanorods via thermolysis of a molecular solid of Fe-complex. *Dalt. Trans.* **2011**, *40*, 8003–8011. [[CrossRef](#)] [[PubMed](#)]
34. Murugappan, K.; Silvester, D.S.; Chaudhary, D.; Arrigan, D.W.M. Electrochemical Characterization of an Oleyl-coated Magnetite Nanoparticle-Modified Electrode. *ChemElectroChem* **2014**, *1*, 1211–1218. [[CrossRef](#)]
35. Bott, A.W. Electrochemistry of Semiconductors. *Curr. Separ.* **1998**, *17*, 87–91. [[CrossRef](#)]
36. Gao, Y.; Hamann, T.W. Quantitative hole collection for photoelectrochemical water oxidation with CuWO<sub>4</sub>. *Chem. Commun.* **2017**, *53*, 1285–1288. [[CrossRef](#)]
37. Bassi, P.S.; Antony, R.P.; Boix, P.P.; Fang, Y.; Barber, J.; Wong, L.H. Crystalline Fe<sub>2</sub>O<sub>3</sub>/Fe<sub>2</sub>TiO<sub>5</sub> heterojunction nanorods with efficient charge separation and hole injection as photoanode for solar water oxidation. *Nano Energy* **2016**, *22*, 310–318. [[CrossRef](#)]

38. Kim, J.H.; Kim, J.H.; Jang, J.W.; Kim, J.Y.; Choi, S.H.; Magesh, G.; Lee, J.; Lee, J.S. Awakening solar water-splitting activity of ZnFe<sub>2</sub>O<sub>4</sub> nanorods by hybrid microwave annealing. *Adv. Energy Mater.* **2015**, *5*, 1–9. [[CrossRef](#)]



© 2020 by the authors. Licensee MDPI, Basel, Switzerland. This article is an open access article distributed under the terms and conditions of the Creative Commons Attribution (CC BY) license (<http://creativecommons.org/licenses/by/4.0/>).